Tunneling and break junction spectroscopy of the ambient-pressure semiconducting and superconducting gap structures in the ladder compound $(Sr, Ca)_{14}Cu_{24}O_{41}$

Toshikazu Ekino,[1,*] Masatoshi Iwano,[2] Akira Sugimoto,[1] Jun Akimitsu,[3] and Alexander M. Gabovich[4]
[1]*Hiroshima University, Graduate School of Advanced Science and Engineering, Higashi-Hiroshima, 739-8521, Japan*
[2]*Hiroshima University, Graduate School of Integrated Arts and Sciences, Higashi-Hiroshima, 739-8521, Japan*
[3]*Okayama University, Research Institute for Interdisciplinary Science, Okayama 700-8530, Japan*
[4]*Institute of Physics, National Academy of Sciences, Kyiv 03680, Ukraine*

(Received 17 October 2020; revised 19 May 2021; accepted 14 June 2021; published 19 August 2021)

The ladder-chain compound $(Sr, Ca)_{14}Cu_{24}O_{41}$ is a semiconductor at ambient pressure, but becomes a bulk superconductor above the pressure of about 3 GPa. Since the compound is at the verge of the metal-insulator transition, it is reasonable to make tunnel measurements to probe the electronic density of states in its subtleties. We present the results of such measurements carried out at ambient pressure. The break junction (BJ) tunneling gives evidence for the apparent typical gap 2Σ of about 140 meV at temperature T, equal to 4 K. The gap is smeared out at $T^* \approx 90$–100 K. We interpret the gap as that induced by the charge density wave (CDW) formation, although its T-dependence differs from the usually observed CDW-like mean-field behavior. Quite unexpectedly, BJ spectra also exhibit distinct zero-bias peak accompanied by the low-energy gaps of $2\Delta \approx 4$–8 meV immediately after BJ are formed at 4 K. The thermally driven disappearance of this apparently superconducting structure at $T_c \approx 7$–13 K is consistent with the conventional properties of superconducting tunnel junctions. The resultant ratio Δ/T_c is consistent with similar observed values for a high-T_c cuprate superconductor. Therefore, we attribute this feature as well as the Josephson-like zero-bias conductance peak to the superconductivity induced at the freshly created BJ surface of the $(Sr, Ca)_{14}Cu_{24}O_{41}$, which is semiconducting in the sample bulk. Our additional scanning tunneling microscopy data testify that the cracked atomic surface of this compound is substantially modified, which might be the reason for the superconductivity appearance.

DOI: 10.1103/PhysRevB.104.054514

I. INTRODUCTION

Oxide $(Sr, Ca)_{14}Cu_{24}O_{41}$ is known as a unique cuprate compound exhibiting pressure-induced superconductivity in the chain-ladder structure [1,2] without CuO_2 planes, being the superconducting area of high-T_c materials (T_c is the superconducting critical temperature) [3]. The crystal structure of $Sr_{14-x}Ca_xCu_{24}O_{41}$ is characterized by two-leg ladders consisting of Cu_2O_3 and chains of CuO_2. Both kinds of rods form a characteristic quasi-one-dimensional crystal structure. The compound concerned was discovered as a byproduct in the synthesis process of $Bi_2Sr_2CaCu_2O_{8+\delta}$ (Bi2212) superconductor. The structure of $Sr_{14-x}Ca_xCu_{24}O_{41}$ can be considered as lying in the intermediate structural region between a two-dimensional square lattice and one-dimensional chain one [3,4]. In this low-dimensional compound, charge carriers self-dope the mother compound $Sr_{14}Cu_{24}O_{41}$ (i.e., $x = 0$), being nevertheless almost localized in the quasi-one-dimensional chains. Therefore, their penetration into the adjacent two-leg ladder structure units is weak.

The doping by Ca leads to the transfer of holes from chains into the ladders. Thus, the metallicity emerges, so that the electric conductivity becomes metallic-like along the ladders, whereas it remains the dielectric-like in the perpendicular direction [3,5,6]. It is rather imprudent to predict superconductivity in specific compounds because no theoretically justified superconducting criteria exist even for elementary superconductors [7–12]. Nevertheless, such an attempt was made in applications to one-dimensional metal oxide ladders on the basis of the t-J model [13]. The emerging Cooper pairing was treated in [13] as the result intrinsic to the $(-U)$ Hubbard metal [14]. This is a phenomenological approach, so that the real origin of the interelectron attraction remained hidden in the system parameters. Fortunately, superconductivity with $T_c = 9$–12 K was indeed found in the chain-ladder compound $Sr_{14-x}Ca_xCu_{24}O_{41}$ under the pressure of 3–5 GPa [1,2,6,15].

The appearance of superconductivity is most probably the consequence of the decreasing conductivity anisotropy and formation of the common infinite two-dimensional Cu-O lattice from the isolated two-leg ladder structures [2]. Indeed, the formal copper valence +2.25 in the mother compound $Sr_{14}Cu_{24}O_{41}$ corresponds to the optimal doping range in CuO_2 layers of cuprate high-T_c superconductors, but in this case it is realized in the almost insulating semiconductor [5]. This is believed to be caused by the carrier localization in the quasi-one-dimensional chains without effective donation of the carriers to the ladders [16].

On the other hand, upon doping bound pairs of holes, which are located at neighboring ladder legs, are randomly distributed at high T. The precursor hole pairs condense into a charge density wave (CDW) state below a certain temperature thus forming the superlattice structures [2,17–19].

*ekino@hiroshima-u.ac.jp

It was established that the CDW states in the studied ladder compounds are not a more or less conventional Peierls transition accompanied by periodic crystal lattice distortions [20–22]. Those CDWs are rather caused by the charge carrier crystallization of hole pairs located in the ladders without detectable lattice distortions (however, it might happen that the distortions are subtle enough and will be found later using a more sophisticated technique, as occurred with tetrathiofulvalinium tetracyanoquinodimethan (TTF-TCNQ) [23]). The Coulomb-interaction-induced crystallization of electrons or holes is a manifestation of the Wigner crystallization predicted for the low-density electron gas [24] and realized here in the anisotropic solid. Magnetism is another player, which influences the electron density of states of the oxide family $Sr_{14-x}Ca_xCu_{24}O_{41}$. In particular, magnetic properties are determined by Cu^{2+} ions with the spin $S = 1/2$. In the insulating Cu_2O_3 ladders, a spin gap of 40–50 meV is observed in the spin excitation spectrum [2,13]. As was noted above, superconductivity or CDWs appear upon doping. Furthermore, the spin gap exists only in the even-leg ladders and quickly decreases with increasing number of the ladder pairs. According to the widespread view previously applied to the whole class of superconducting cuprates [25–27], the charge carriers inserted into even-legs ladders can form Cooper pairs glued by antiferromagnetic spin correlations [28]. Therefore, the study of $Sr_{14-x}Ca_xCu_{24}O_{41}$ is worthwhile, in particular, to confirm or reject the purported spin-fluctuation mechanism of superconductivity emerging in CuO_2 layers.

In this paper, we report on the measurements of the $Sr_{14}Cu_{24}O_{41}$ properties by means of the tunneling spectroscopy. The initial aim of the experiments was to find and analyze the energy gaps in the quasiparticle spectrum of the semiconducting state as well as to probe surface atomic structures of the ladder-like crystal lattice. For this purpose, the break-junction tunneling spectroscopy (BJTS) technique was introduced to detect fragile surface electronic states [29,30]. The scanning tunneling microscopy/spectroscopy (STM/STS) was employed to directly image the crystal surface at the atomic resolution, which was successfully used, continuously improving its performance [31,32].

The high content of Ca $x = 11.5$ was found suitable for BJTS because then the electrical conductivity becomes high enough. At the same time, the hopping transport activation energy becomes as low as a few meV [2], so that the gap structures can be easily revealed in tunnel current-voltage characteristics. Our STM topographical images showed that the atomic arrangements are substantially modified at the surface.

Perhaps the most intriguing and unexpected result of the present work is the observation of superconducting features at the BJ interfaces. This phenomenon has been never observed in the bulk crystal at ambient pressure, although it was obtained under the high-pressure influence [1,2]. Since $(Sr,Ca)_{14}Cu_{24}O_{41}$ contains no atoms of ambient-pressure elementary superconductors [11,33], the observed interface superconductivity is intrinsic to the modified surface of the bulk crystal. Therefore, we suggest that the conducting Cu-O networks forming both the ladder and chain one-dimensional rods along the crystal c-axis are crucial to induce the local surface superconductivity with the atomic arrangements being different from those of the CuO_2 cuprate layers [34,35]. The results are outlined and discussed in subsequent sections.

In general, surface electronic properties are different from their bulk counterparts [36–39]. This is due to the loss of lattice periodicity so that the potential wells for the quasiparticles near the surface are different from the bulk state ones and, in particular, dangling bonds appear. Moreover, the surface atoms are subject to the equilibrium relaxation and reconstruction [36–40]. The surface as a whole inevitably includes a huge surface dipole, which is significant for both insulators and metals [37,41–43]. The electron density redistribution occurs not only in the upper atomic layer but in several adjacent lower layers as well. It is remarkable that Faraday recognized those simple facts many years ago for the very important particular case of water ice [44] (see also more modern accounts of the relevant phenomena [45,46]).

The crystal truncation leads also to the existence of the intrinsic surface electron states, which, depending on the nature of the electron bond in the bulk, are called Tamm [47] or Shockley [48] states, although their origin is essentially the same [37,39,49,50]. Defects or impurities, which always exist on oxide surfaces [51], may lead to extrinsic surface states [37,39]. Finally, image force-induced localized states are also inevitable near the interfaces. They are located close to the solid when the localized states are located near a metal [52].

It is natural to suggest that the electron spectrum modifications near the surface may lead to a specific surface superconductivity, which is especially interesting in the pure case when bulk superconductivity is absent. The first proposal in this direction was made by Ginzburg and Kirzhnits more than 50 years ago [53,54]. It is necessary to emphasize that here and in related works the standard mean-field Bardeen-Cooper-Schrieffer (BCS) state [55,56] is assumed rather than the two-dimensional fragile Berezinskii-Thouless-Kosterlitz (BKT) quasi-order [57]. The BKT quasi-order was later on discovered experimentally but it seems not to be relevant in this context. Some other possible kinds of surface superconductivity are discussed below in connection to our results.

II. EXPERIMENT

The application of the hydrostatic pressure compresses a sample, while the break junction is formed after expansion and fracturing of the crystal, in which it is elongated along certain axes contrary to the compression in the pressurized measurements. Single crystals were synthesized by the traveling solvent floating zone method [58]. The main technique applied here to study gap features is the BJTS. The low-temperature ultra-high-vacuum (UHV) STM/STS was also used as supplementary measurements to resolve atomic arrangements. In the BJTS consisting of a superconductor, clean unaffected superconductor-insulator-superconductor (S-I-S) junction interfaces were obtained *in situ* along the crack of tiny single-crystal piece at temperatures below T_c. The measurements were successful. In particular, the nominally symmetric BJ configuration enabled to reveal the gap-edge-related peak structures in the conductance G versus voltage V, curve $G(V) = dI/dV(V)$ with the peak-to-peak distance $V = 4\Delta/e$, where I, 2Δ, and e denote the tunnel current, the energy gap and the elementary charge, respectively [59,60].

However, sometimes in the same BJ setup, the peak-to-peak distance is $V = 2\Delta/e$, which is appropriate to superconductor-insulator-normal metal (S-I-N) junctions. A similar gap feature was found for the energy gap Σ, which has a CDW nature.

For a mechanically stable BJs, a long-period full bias-voltage scan taking ∼20 min or more was mainly adopted using the low-frequency ac-modulation technique with the lock-in amplifier. The present STM apparatus is an upgraded Omicron low-temperature ultra-high-vacuum LT-UHV-STM system. The sample was cleaved *in situ* in the LT-UHV chamber under the pressure of $\approx 10^{-8}$ Pa to avoid atomic migrations on the crystal surface. The tunneling Pt/Ir tip was used. Its surface was processed by a high-voltage field emission cleaning with Au target. The STM measurements were carried out in the temperature range 4.9–300 K under the UHV condition with the pressure of $\approx 10^{-8}$ Pa. The STM images were obtained in a constant-current mode.

III. RESULTS AND DISCUSSION

As was mentioned in the Introduction, the present BJTS clarifies the existence of not only the semiconducting gap but also the gap originated from superconductivity at the BJ interface. We expected to observe the semiconducting gap in the ladder compound and observed, but the emerging superconductivity appeared to be an unexpected phenomenon because it was not found earlier in the bulk. Therefore, data describing the semiconducting gap are discussed at first as a significant priority and are followed by the evidence for surface superconductivity.

A. CDW manifestations

Prior to BJTS experiments, T dependence of the resistivity ρ, was measured as is shown in the inset to Fig. 1. The curve $\rho(T)$ exhibits an upturn below ∼60 K with no saturation down to 4.2 K. This indicates that the electric transport is predominantly metallic and takes place mostly along the ladder direction (c-axis), although there is a small admixture flowing in the a-direction, which agrees with previous measurements carried out both at ambient and high pressure [6]. The activation energy of ∼1 meV at low T indicates that the bulk transport gap almost disappears for this Ca content, which is consistent with the data published previously [1,4]. The solid curve in the main frame of Fig. 1 shows the representative BJTS conductance $G(V)$ of $Sr_{2.5}Ca_{11.5}Cu_{24}O_{41}$ at 4.2 K. The junction was stable enough while scanning the whole spectrum in spite of the mechanically formed junction. We discussed hereafter only such tough junctions. In measuring the semiconducting tunnel junction conductance, the sample resistance cannot be ignored as opposed to the superconducting case where the sample resistance is zero. In the present data, the high-bias background conductance is ∼10 mS. The corresponding resistance of about 100 Ω and >1 kΩ at lower biases is much higher than the bulk sample resistance including the contact resistance of about ∼10 mΩ. Hence, the observed BJ tunnel resistance is determined by the tunneling barrier rather than by the bulk sample resistance. It means that the voltage drops mainly in the tunneling barrier and the

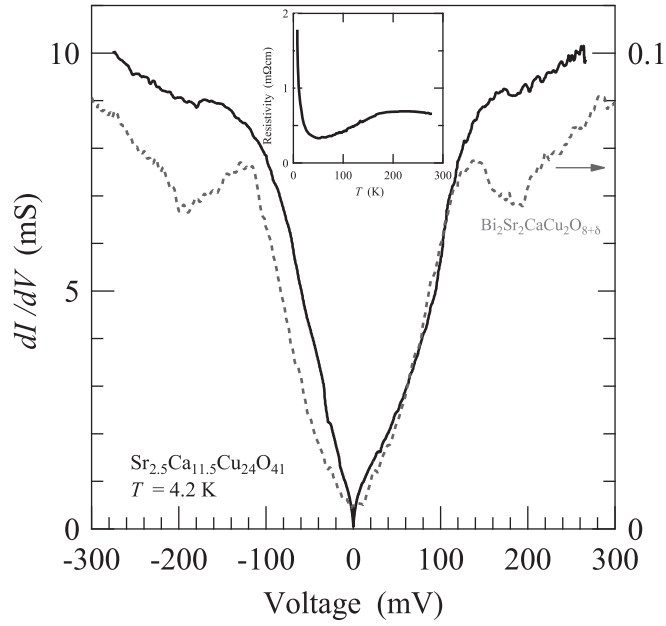

FIG. 1. Break junction (BJ) tunneling conductance $G(V)$ for the ladder compound $Sr_{2.5}Ca_{11.5}Cu_{24}O_{41}$ revealing the largest gap structures at ±160–170 mV (solid curve). The broken curve represents BJ conductance $G(V)$ for $Bi_2Sr_2CaCu_2O_{8+\delta}$ (Bi2212) as a material in which the normal-state gap is well known to exist. Inset shows the temperature dependence of electrical resistivity.

characteristic conductance structures describe the electronic density of states. The asymmetry may indicate that the BJ crack occurs inside the nonstoichiometric region of the crystal. The broadened gap-edge peaks are evident at ±160–170 mV $= \pm 2\Sigma/e$, which are the largest gap energy found in our measurements. Here, 2Σ represents the semiconducting (Sm) gap. Notwithstanding the asymmetry of the $G(V)$ curve, we believe that the observed gapped region corresponds to the symmetric semiconductor-insulator-semiconductor junction of the BJ tunnel junction. For instance, such asymmetrical smeared dependencies are characteristic of tunnel spectra for CDW layered dichalcogenides [61].

The broken curve shows the representative pseudogap conductance of as grown, slightly overdoped ($T_c = 86$–89 K) $Bi_2Sr_2CaCu_2O_{8+\delta}$ (Bi2212) superconductor crystal at 4.2 K obtained from our BJTS measurements [62–64]. In those publications, we attributed the larger gap in Bi2212 to the CDW semiconducting gap in accordance with other experiments and theoretical considerations [65–68]. The gap edges occur at almost the same energies, and the subgap linear conductance behavior is commonly seen inside the gap region. This similarity suggests that the energy scale is determined by the characteristic Cu-O conducting networks, regardless of the difference in the crystal structures, crystal lattice anisotropy, and electronic configuration details. The broadening of the CDW gap peaks in the ladder compound is larger than those of Bi2212 [63]. Such a broadening characterizes the tunnel conductance, which has been calculated and discussed in terms of the intrinsic spatial disorder [69]. In particular, the calculation applied to Bi2212 reproduces well the experimental data attributing larger gap features to CDW manifestations.

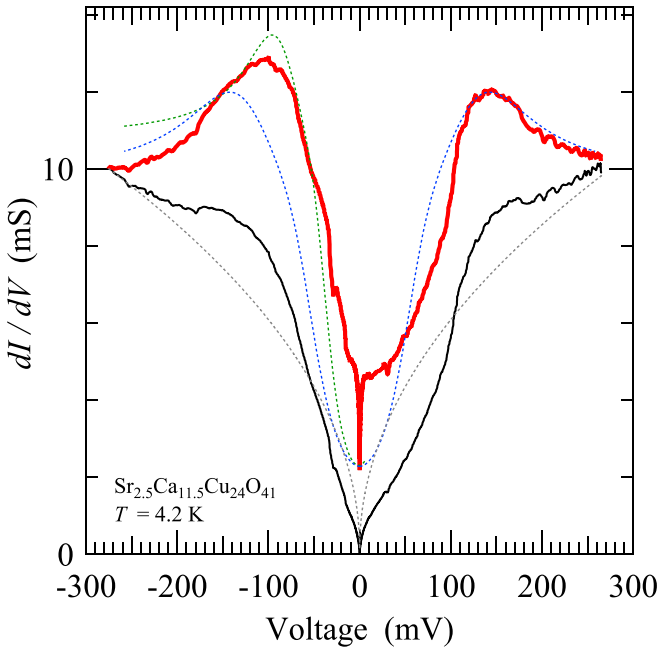

FIG. 2. The raw conductance $G(V)$ (thin solid curve from Fig. 1) and the normalized conductance $G(V)/[|V|^{1/2}+0.25]$ (thick solid curve) fitted by the thermal smeared density of states $N(E, \Sigma_{\rm fit}, \Gamma)$ at $T = 4.2$ K with quasiparticle broadening (broken curve, $\Sigma_{\rm fit} = 63$ meV and $\Gamma = 35$ meV). The negative bias fitting (dot-dashed curve) corresponds to $\Sigma_{\rm fit} = 42$ meV and $\Gamma = 22$ meV.

The characteristic cusp-like dip at zero bias in the ladder compound below ± 10 meV was never observed in the Bi2212 pseudogap depression. The cusp dependence $G(V) \sim |V|^{\alpha}$ ($\alpha < 1$) may signal [70,71] charge accumulation, weak localization, or/and electron-electron interaction [72–74] at the junction interface region reflected in the tunneling conductance as a spectrum background in $Sr_{2.5}Ca_{11.5}Cu_{24}O_{41}$. The Fermi surface anisotropy and imperfectness of nesting may also lead to additional features in $G(V)$ in addition to those described by the mean-field Bardeen-Cooper-Schrieffer (BCS) like behavior [75,76]. Both the characteristic low-energy feature of $G(V)$ and the peak broadening, which manifest themselves in Fig. 1, are consistent with such interpretations. There exits an additional extrinsic possibility that the conductance being a convolution of the semiconducting density of states from both electrodes is modified because of the crystal surface distortion due to the strong electric field in the tunnel junction [77,78].

In any case, when the raw data for $G(V)$ from Fig. 1 are divided by the background conductance $|V|^{1/2} + c$ (c is a fitting constant to suppress zero-bias divergence) [75,76], then the normalized conductance have the form of the broadened BCS density of states,

$$N(E, \Sigma_{\rm fit}, \Gamma) = {\rm Re}\left\{(E - i\Gamma)/\sqrt{(E - i\Gamma)^2 - \Sigma_{\rm fit}^2}\right\}. \quad (1)$$

This is the standard phenomenological Dynes formula originally applied to superconductors [79]. Here, $\Sigma_{\rm fit}$ and Γ are the fitting CDW gap and the quasiparticle-lifetime broadening parameter, respectively. Figure 2 shows the conductance raw data together with the normalized conductance described by Eq. (1) for Sm-I-Sm geometry, where I denotes an insulator. The gap–edge peaks and the conductance leakage become more apparent and understood after the normalization and the subsequent fitting. The difference in the gap peak positions for different bias polarities in the normalized data can be easily seen, although in the raw data they seem to be almost symmetric. The fitting value $\Sigma_{\rm fit} = 63$ meV is almost consistent with that obtained from the peak-to-peak distance $eV_{p\text{-}p}/4 = \Sigma = 60$–$75$ meV. The calculated curves well reproduce the experimental data, thereby demonstrating that the ladder-compound dielectric gap can be described in the mean-field manner.

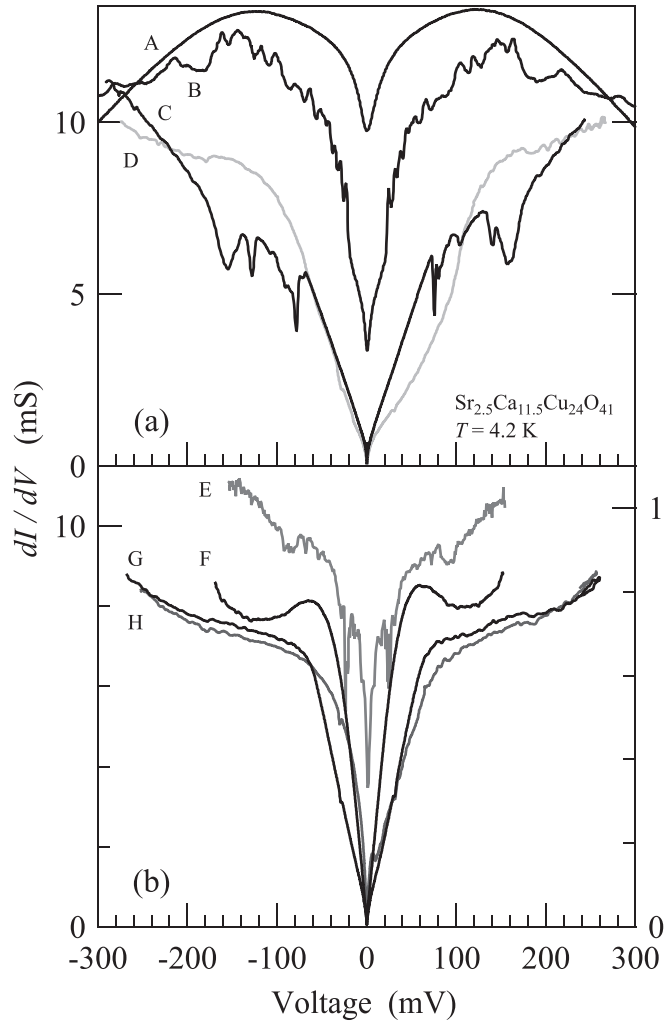

FIG. 3. (a) The conductance-voltage characteristics $G(V)$ for different $Sr_{2.5}Ca_{11.5}Cu_{24}O_{41}$ BJs (curves A to C), demonstrating the characteristic gap energy almost similar to that for D from Fig. 1. (b) $G(V)$ with the gap voltages twice lower than (a) (E to H). Such $G(V)$ appear along with those from panel (a). All the curves demonstrate the reproducible dominant peaks located at $\pm 2\Sigma/e \approx \pm 130$–$170$ mV in (a) as well as smaller secondary peaks at ± 60–80 mV in (b) with additional fine structures over the whole bias range especially in B, C, and E.

In Fig. 3, conductance-voltage characteristics are demonstrated for different BJs. Although the overall conductance shapes are different among the junctions, the characteristic peak biases are kept almost at the same positions. The predominant peak positions are mainly located at

±130–170 mV, which can be regarded as an inherent material property. The scattered values are most probably due to the inhomogeneous distributions of the local Sr content substituting Ca and/or slight crystallographic difference, thus resulting in a modification of the characteristic energy. The gap-edge biases do not shift away even when the spiky subgap structures blur the picture. The noticeable fine spike structures extend to hundreds of mV as is seen from Fig. 3(a). Those discontinuities in the current voltage characteristics can be primarily due to local superconducting patches at the interface, which will be discussed in the next section. We also observed the noticeable peaks or shoulders at twice-lower biases ±60–80 mV such as C in Fig. 3(a). The typical examples are shown in Fig. 3(b). Two groups of the peak-to-peak values in the ranges 260–340 mV in Fig. 3(a), and 130–170 mV in Fig. 3(b) most probably come from Sm-I-Sm ($4\Sigma/e$) and Sm-I-N ($2\Sigma/e$) junctions, respectively, as can be guessed by analogy with the results for superconducting tunnel junctions [59,80]. We attribute smaller gaps 130–170 mV to the mechanically damaged BJ interfaces, which form Sm-I-N junctions. It happens when CDW states are destroyed in the surface region of one of the electrodes. Another possible reason of the smaller gap appearance is the gap anisotropy, which was suggested in transport measurements along different crystallographic axes (see Fig. 1 of Ref. [6]). We note that the gap values $2\Sigma = 130$–170 meV correlate with those inferred from optical conductivity measurements of nondoped $Sr_{14}Cu_{24}O_{41}$, in which CDW gaps were detected [17,18]. Since the CDW gap-related bias positions of two kinds are almost reproduced within the range of <15%, one sees that the sample resistance and the resistance of contacts do not seriously affect the measurements, which confirm the validity of our interpretation.

Bulk electric transport measurements demonstrate that the activation (CDW) gap equals 3 meV for Ca content $x = 9$ and disappears for larger x [2,18]. Hence, broad conductance peaks in BJs centered around the bias in the range 130–170 mV, corresponding to CDW gaps for the material with $x = 0$, should be considered as a manifestation of CDW gap spatial distribution due to the intrinsic sample inhomogeneity (see, e.g., calculations for Σ distribution in cuprate BJs [64]). Random doping with Ca atoms makes samples electronically inhomogeneous. Consequently, one sees that, although such doping increases the leakage conductance, the main CDW peak positions are almost unchanged with x up to $x = 11.5$. Formally, the optimum charge carrier concentration is about +0.25 per Cu atom for the undoped $Sr_{14}Cu_{24}O_{41}$, although the carriers are almost localized [5]. This value is similar to that for cuprate superconductors [81]. Our observation of the normal-state gap in the chain-ladder compound in the case of large doping concentrations qualitatively agrees with the persisting partial CDW gapping even in the optimally doped high-T_c compositions of Bi2212 [22,64].

The temperature evolution of the tunnel $G(V)$ is shown in Fig. 4. The overall T-evolution is similar to what is observed in the chalcogenide compounds with CDWs and to the behavior of pseudogaps in high-T_c oxides [82–84]. Temperature shifts of the gap-related peak positions are well noticeable up to the temperatures where the gap structure is almost smeared out in the more or less conventional mean-field manner. Traces

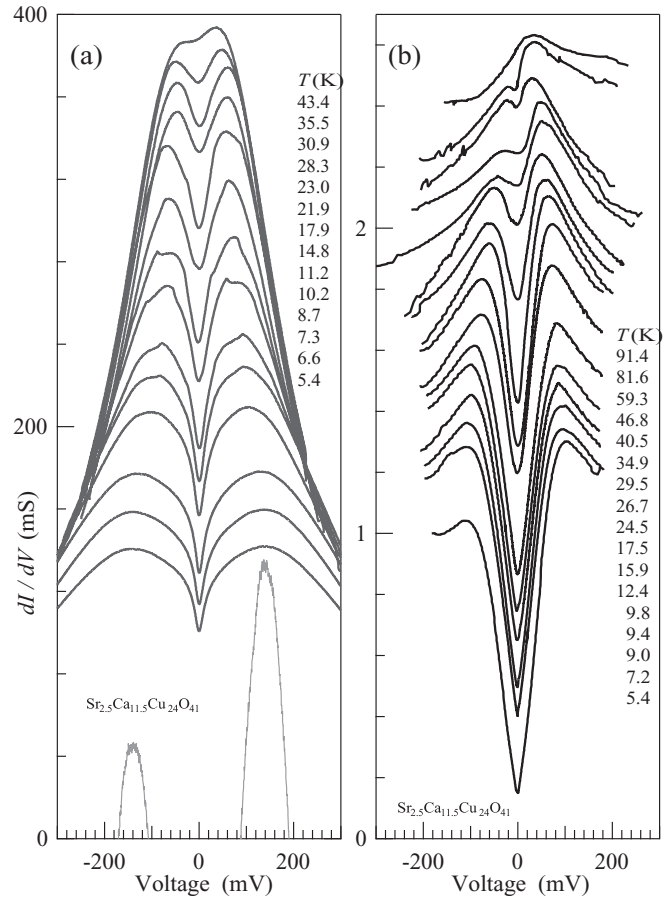

FIG. 4. Temperature, T, dependencies of $G(V)$, obtained for different BJs ((a), (b)) from the same crystal batch. (a) corresponds to Fig. 3, curve A, while (b) describes BJ with a slightly smaller low-T gap value. The gap value can be determined through the peak positions as shown by the vertically magnified curve in (a).

of subgap features are seen in Fig. 4(a) at positions decreasing with T and dying out well below the disappearance of the main peaks. It should be noted that the main peak also splits at intermediate temperatures. Such behavior can be explained if we assume that (i) the conductance curve is an average of contributions from several current paths and (ii) asymmetric junction configurations participate in the formation of this collective averaged $G(V)$ [64]. At the same time, $G(V)$ in Fig. 4(b) shows the single gap feature at ±110 mV with the asymmetry in the conductance magnitude, which increases with T. The corresponding gap value is slightly smaller than 140 meV of Fig. 4(a).

Upon warming, the gap features of $G(V)$ in Fig. 4(a) could not be traced up to its closing T because of the thermomechanical instability of this junction. However, it might be extrapolated that the asymmetric peak structure would disappear at higher temperature, leaving the CDW-free convex background. On the other hands, the junction shown in Fig. 4(b) is fairly stable up to even above 90 K, where the gap structure almost disappears leaving a broad hump centered at the positive bias. Such a hump is similar to that observed above the gap-disappearance temperature in the BJTS made of cuprate superconductors [62,83]. The origin of the broad

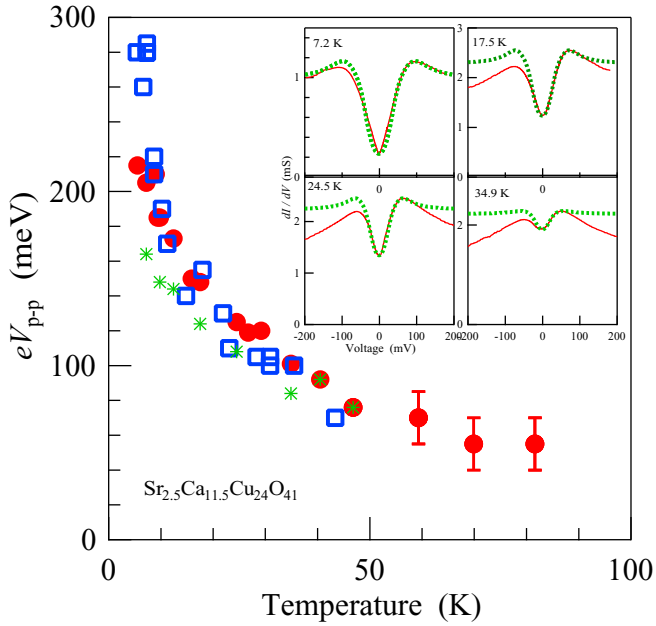

FIG. 5. T dependencies of the 4Σ values determined from the peak-to-peak bias separation in $G(V)$. Open squares and filled circles correspond to data obtained from Figs. 4(a) and 4(b), respectively. Insets show the fitting results of $G(V)$ in Fig. 4 using the thermal smeared $N(E, \Sigma_{\rm fit}, \Gamma)$ [Eq. (1)]: $T = 7.2$ K ($\Sigma_{\rm fit} = 41$ meV, $\Gamma = 26$ meV), 17.5 K (31 meV, 19 meV), 24.5 K (27 meV, 18 meV), 34.9 K (21 meV, 21 meV). Gap values determined by fitting are indicated in the main frame by asterisks.

background conductance hump might involve the magnetic moments from Cu spins at the junction interface region [85]. The extrinsic Joule heating effect in the junctions seems to be unlikely because it would produce the symmetric $G(V)$ shape with respect to zero bias contrary to the present cases. Both the observed offset of peak position and the difference in $G(V)$ magnitude between the bias polarities can be a result of the tunnel barrier asymmetry in randomly cracked samples [86]. It can be also due to the formation of the Schottky barrier at the interface of the ladder compound, in which the tunnel barrier thickness depends on the bias voltages due to a formation of the depletion layer at the semiconducting interface [87,88].

Temperature dependencies of the gap energies determined from Fig. 4 are plotted in Fig. 5. The gap values 4Σ are directly determined from the peak positions (eV_{p-p}) in $G(V)$ curves as is shown at the bottom of Fig. 4(a). This procedure is valid without significant ambiguities up to high temperatures when the gaps disappear altogether. Their values determined at 4.2 K are widely distributed in the range of 200–300 meV. Above ≈10 K they almost converge, indicating that the statistical gap distribution narrows. The gap value decreases steeply up to ≈30 K followed by leveling off at higher temperatures, giving rise to the concave curve in the whole T range. A dependence of this kind is in apparent contrast to the standard mean-field BCS-like T-dependence, whatever the microscopic origin of the order parameter.

To elucidate whether the apparent peaks are the coherent ones and reflect the temperature evolution of the dielectric gap, the $G(V)$ curves were fitted at each temperature. The quasiparticle density of states $N(E, \Sigma_{\rm fit}, \Gamma)$ given by Eq. (1) was chosen as the appropriate candidate for the analysis, as has been already mentioned in Fig. 2. The insets in Fig. 5 show the fitting results by the thermal smeared $N(E, \Sigma_{\rm fit}, \Gamma)$ for raw $G(V)$ curves at selected temperatures. The calculated curves describe the observed $G(V)$ well, especially in the subgap bias region by tuning the values of $\Sigma_{\rm fit}$, Γ and the conductance leakage $G(0)$ at each T. Disagreement between the values at the opposite biases and the discrepancies at higher biases are most probably due to the bad knowledge of the background behavior, which is unfortunately inevitable as was discussed elsewhere [64,70,88,89]. Nevertheless, the $\Sigma_{\rm fit}$ values obtained by the fitting procedure almost coincide with the gap values from the $G(V)$ peak biases with the deviation of ∼10–20% at temperatures of the steepest changes in the gap value below ∼50 K. This difference is concomitant with the broadening effect reflected by Γ, although its microscopic origin is not clear. We note that the thermal smearing of the gap structure should be negligible here because thermal energies are much smaller than the gap ones (∼12 meV). Therefore, one can make the conclusion that the peak bias position in $G(V)$ corresponds to the gap value from $N(E, \Sigma_{\rm fit}, \Gamma)$ regardless of the gap formation mechanism. As a result, we are forced to infer that the dielectric gap thermal evolution substantially differs from the mean field BCS-like behavior.

Specifically, conventional superconducting, dielectric, or magnetic order parameters decrease rapidly in the vicinity of the critical temperature [21,22,64,80,82,90]. On the other hand, the semiconducting gap T dependence demonstrated in Fig. 5 was found in the Kondo compounds, where no long-range order develops, so that the mean-field picture of the phase transition fails [30,91]. Similar deviations from the mean-field behavior were found for the CDW (Peierls) gaps in $K_2Pt(CN)_4Br_{0.3}3H_2O$ (KCP) [92,93]. It is remarkable that the three-dimensional mean-field T-dependence of the dielectric order parameter in KCP is restored under the pressure when fluctuations are suppressed [94]. The quoted experimental data for different materials undergoing metal-insulator transitions are well described by the phase transition theory taking into account the order parameter fluctuations enhanced by the low dimensionality of the objects [95–98]. In our case, the enhanced suppression of the CDW order parameter at higher temperatures (see Fig. 5) is consistent with the fluctuation-driven scenario. Moreover, in the high-T region, where fluctuations are well developed, the very notion of the phase transition critical temperature loses its meaning. This is also clearly seen in Fig. 5 as the flattening out of the $\Sigma(T)$ dependence.

Let us estimate the ratio $2\Sigma(0)/T^*$ characteristic of BCS-like models. Here, $T^* \approx 90$ K is the gap-closing temperature, which cannot be unequivocally identified with the mean-field critical temperature due to reservations concerning its definition (see above). The low-T gap value of 4Σ in Fig. 5 is about 220–290 meV, so that the ratio $2\Sigma(4\ {\rm K})/k_BT^*$ is within the range 14–19 (k_B is the Boltzmann constant). It substantially exceeds the BCS value $2\pi/\gamma \approx 3.53$ for s-wave superconductors [56,80,90]. Moreover, it is even larger than its counterpart values 9–14 for such conventional CDW materials as $NbSe_3$, the overall T-dependence of Σ also being quite different [82,90,99].

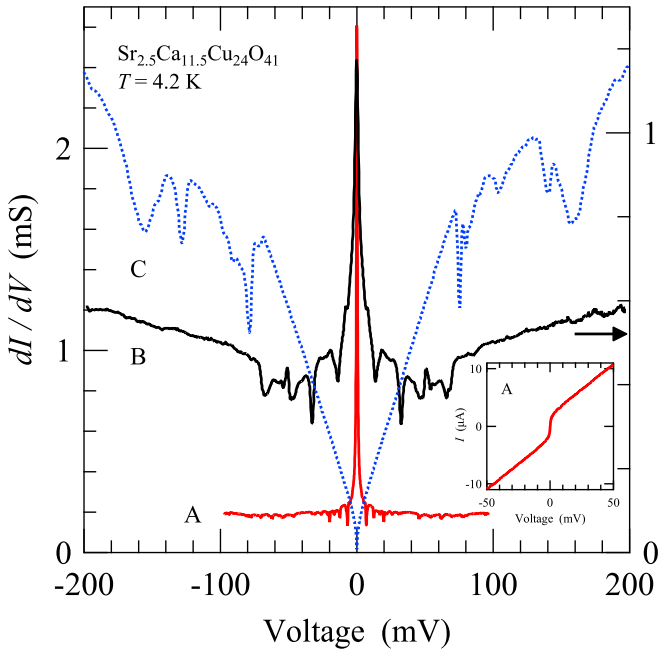

FIG. 6. BJ conductance $G(V)$ at 4.2 K for samples demonstrating sharp zero-bias peaks (A, B). Curve B shows the gap-edge structure at $\pm \approx 70$ mV. $G(V)$ for curve C (Fig. 3 C) reveals gap-edge peaks at the same bias voltages, being half of those corresponding to the main gap-edge peaks at $\pm \approx 140$ mV. The intensity of zero-bias peak correlates with the reduction in the CDW-gap-related structures as can be seen by comparing curves A and B. Inset shows the I–V characteristics for A.

B. Superconductivity appearance

The break junction spectra presented in Figs. 1 to 4 demonstrate the semiconducting features attributed to the CDWs [2,100]. As has been indicated above, $Sr_{2.5}Ca_{11.5}Cu_{14}O_{24}$ crystals can become superconducting as well with another kind of the electron spectrum gapping. It occurs, however, only under a hydrostatic pressure larger than 3 GPa [1,2]. Nevertheless, our tunnel BJ experiments, which probe the sample surface, reveal ambient pressure superconductivity manifestations for some junctions. In Fig. 6, the results of such $G(V)$ measurements are shown for curves A and B. Specifically, intensive zero-bias peaks are clearly seen in those conductance-versus-voltage curves.

In a conventional manner, we interpret the zero-bias vertical spikes appearing in A and B as the dc Josephson effect [56,60,80,101]. Since a BJ is formed by applying a tensile force to a fixed thin crystal piece 0.2–0.3 mm thick and cracking it in a direction perpendicular to the a-c plane, the crystal expands rather than compresses before the fracture. This should result in an effect equivalent to the application of the uniaxial negative pressure. Therefore, the zero-bias peaks cannot be attributed to the bulk superconductivity under pressure found earlier [1,2].

In curve A, an intensive zero-bias peak is observed in the bias range of ± 100 mV. The I-V characteristics by itself shown in the inset is qualitatively similar to that of the tunnel junction shunted by external resistance, demonstrating the smeared I-V appearance around zero bias [102]. From the approximate value of the critical current $I_c \sim 1\ \mu$A in zero-bias vertical region of I-V characteristics and the high-bias resistance $R_N \approx 5.2$ kΩ, and assuming the tunnel nature of I_c, the superconducting gap can be estimated as $\Delta = 2eI_cR_N/\pi \approx 3.3$ meV [103]. This value is almost consistent with the directly measured Δ from tunneling characteristics, which is described below. This fact is, however, in contrast to the empirical inequality $I_cR_N \ll \Delta/e$ for the typical cuprate superconductors [104]. The later effect is most probably due to the detrimental influence of CDWs on I_c, which is especially large when the CDW-gapped sector on the Fermi surface becomes significant, as in the case for cuprates [22,64]. In the Ambegaokar-Baratoff isotropic basic model [103], the Josephson critical current is reduced by a factor of $(1-\mu)^2$, where μ denotes the relative share of the Fermi surface, where the CDW gap emerges [105]. In the case of d-wave superconductivity and with account of the tunneling directionality, the reduction was shown to be similarly important but cannot be given by such a simple formula [106]. At the same time, R_N is inferred from data for large biases, where the effects of both Δ and Σ die out, so this is a true "normal-state" quantity. It seems that for the ladder-chain compounds the CDW-gapped part of the Fermi surface is comparably smaller, so that I_c decrease may be neglected for rough estimations.

Curve B of Fig. 6 shows that the zero-bias peak coexists with the CDW manifestations, as is well known to occur in various classes of materials [21,22]. The structures at $\pm \approx 70$ mV in curve C are followed by the main peak structures at $\pm \approx 140$ mV. However, in curve C, a deep V-like zero-bias minimum is observed instead of Josephson peaks inherent to curves A and B. The CDW-related kinks are conspicuous at ± 70 mV in curve B and are located at the same biases as the peak-dip structures of curve C [Fig. 3(a) C]. This is half the value of CDW-gap bias voltages observed at $\pm 2\Sigma/e \approx \pm 140$ mV, although no trace of the structures at those locations can be found in curve B. Therefore, it seems that the intensity of zero-bias peak accompanies a decrease in the main gap structures at higher biases. The appearance of half the CDW gap value in curve B indicates the existence of damaged junction interfaces, which can cause the zero-bias peak as a manifestation of the local superconductivity at those interfaces.

To study the superconductivity found at the surfaces of cracked crystals, we further investigated $G(V)$ at low bias voltages and $T = 4.2$ K. The results are depicted in Fig. 7. Curve A reveals a zero-bias peak, most probably of the superconducting origin as a Josephson effect, from which this BJ is attributed to an S-I-S junction. It is reasonable to identify the main peaks at ± 4 mV as induced by the superconducting gapping, whereas 4 meV approximately equals to 2Δ. On the other hand, for curve B from different BJ, the absence of both the zero-bias peak and fine structures suggest the identification of this $G(V)$ with the S-I-N junction having the peak location at $\pm\Delta/e$. Coexistence of 2Δ and 4Δ peak-to-peak distances in BJs was frequently observed and is due to the inhomogeneity of the cracked surfaces and randomness of the current paths [64,70,107,108].

It looks that the superconducting energy gaps Δ inherent to curves A and B of Fig. 7 are of different magnitudes. However, since the direct comparison of the Δ values from the broadened curve B and multiple-feature curve A seems ambiguous, we tried to model them on the basis of the formula

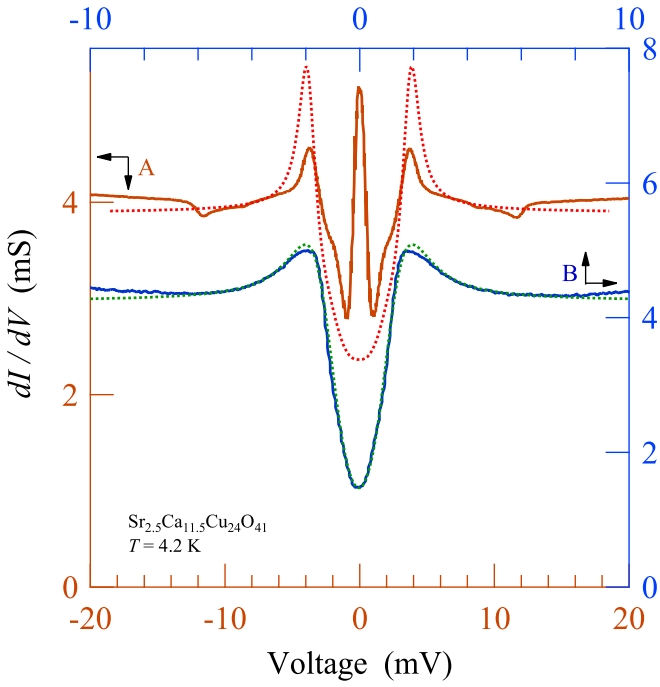

FIG. 7. $G(V)$ of the $Sr_{2.5}Ca_{11.5}Cu_{24}O_{41}$ BJ in the low bias region. Curves A and B correspond to the superconductor-insulator-superconductor (S-I-S) and superconductor-insulator-normal metal (S-I-N) junctions, respectively. Curve A demonstrates the zero-bias Josephson peak together with the gap-related structures at $\pm \approx 2$ mV and ± 4 mV, shallow dips at ± 8 mV and ± 12 mV. Curve B demonstrates the broad gap maxima and a depression at zero bias. The dotted curves represent fitting using the thermal smeared $N(E, \Delta_{\rm fit}, \Gamma)$ [Eq. (1)] for A [S-I-S, $\Delta_{\rm fit} = 2$ meV, $\Gamma = 0.4$ meV, additional leakage of half the background $G(V)$] and B (S-I-N, $\Delta_{\rm fit} = 1.3$ meV, $\Gamma = 0.25$ meV, no additional leakage) junction geometries, respectively.

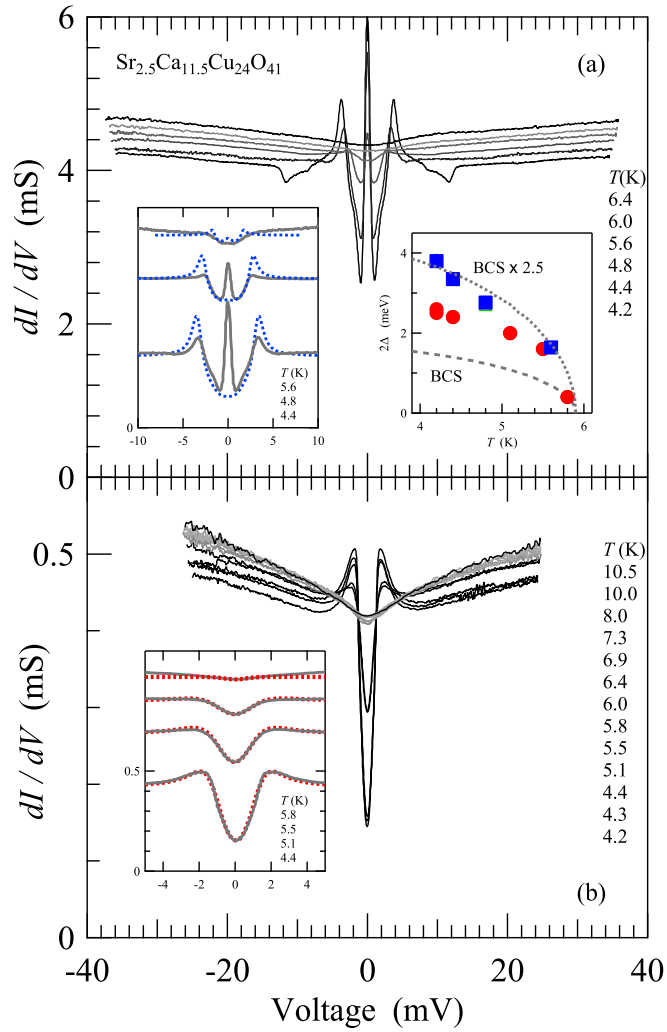

FIG. 8. T evolution of conductances A and B of Fig. 7 presented in panels (a) and (b), which are attributed to S-I-S and S-I-N junction geometries of break junction, respectively. The broken curves of left insets for (a) and (b) show the fitted $G(V)$s with thermal smeared Eq. (1) (using $\Delta_{\rm fit}$ instead of $\Sigma_{\rm fit}$) for (a) S-I-S and (b) S-I-N geometries, respectively, using the same procedure as Fig. 7. Temperature dependence of the superconducting gap 2Δ is demonstrated in the right inset of (a), together with the BCS dependence [80]. Squares and circles correspond to (a) and (b), respectively.

$N(E, \Delta_{\rm fit}, \Gamma)$ [79], where $\Delta_{\rm fit}$ is the fitting value of the superconducting gap instead of $\Sigma_{\rm fit}$ from Eq. (1). Unfortunately, the multiple-gap character in the S-I-S junction prevented us from fitting for the simple convolution of the densities of states. Therefore, we fitted the S-I-S convoluted densities of states using the gap-peak energies for curve A [79]. The procedures led to the gap values of $\Delta_{\rm fit} = 2$ meV and 1.3 meV for S-I-S and S-I-N junctions, respectively. The smaller value for S-I-N can be retrieved if we consider the empirical renormalization effect of Γ added to $\Delta_{\rm fit}$ for the S-I-N superconducting tunneling [107,108]. It should be noted that the quasiparticle density of states was well fitted by the original weak-coupling BCS model, assuming the s-wave pairing symmetry of the superconducting order parameter. Nevertheless, it would be premature to make firm statements about the actual symmetry of the latter. Anyway, if the superconducting order parameter symmetry is a purely d-wave one, the incoherent tunneling in the sprit of the Ambegaokar-Baratoff model will average out the Josephson current between broken crystal pieces, so that the directionality of tunneling should be assumed to obtain the nonzero result [60,109,110].

Figure 8 shows temperature evolution of $G(V)$ presented in Fig. 7 for $T = 4.2$ K. Both sets of curves demonstrate the behavior of S-I-S and S-I-N junctions involving BCS superconductors [80]. Namely, the coherence peaks are suppressed and the peak-to-peak distance narrows with increasing T. The gap structures disappear and merge with the background at critical temperature $T_c \approx 6$–7 K. It seems that this behavior together with the observation of the Josephson-like supercurrent proves that we are dealing with the genuine superconductivity in this ladder-chain oxide. In the insets of Fig. 8, the calculated $G(V)s$ for S-I-S [Fig. 8(a)] and S-I-N [Fig. 8(b)] junctions by $N(E, \Delta_{\rm fit}, \Gamma)$ [Eq. (1)] are shown together with the T-dependence of the gap values. One sees that the gap values are larger than the BCS but the description by the s-wave BCS T-dependence is satisfactory. Nevertheless, measurements in the external magnetic field as well as the measurements at much lower T are needed to provide further confirmation of superconductivity.

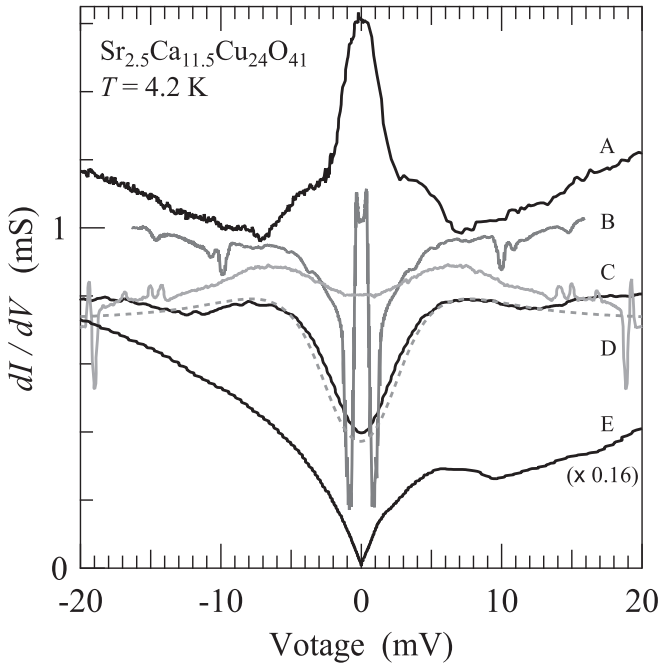

FIG. 9. $G(V)$ from different BJs at 4.2 K demonstrating a reproducibility of the superconducting gap related features in the BJ interface. Curve A possesses the zero-bias hump below ±7 mV. In curves B, C, and D, broad peaks at ±7 mV correspond to the outer minima locations of A. Curve E is a bias close-up version of Fig. 3 H. The dotted curve corresponds to the thermal smeared $N(E, \Delta_{\text{fit}}, \Gamma)$ [Eq. (1)] for the S-I-S junction with $\Delta_{\text{fit}} \approx 3$ meV $\gtrsim \Gamma$.

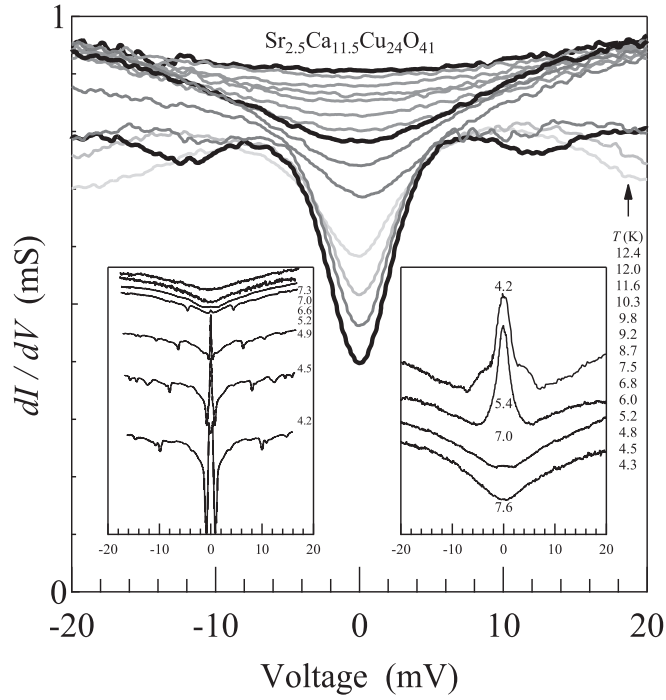

FIG. 10. Temperature evolution of $G(V)$ for BJs showing the superconducting gap, whose low-T characteristics are shown in Fig. 9. The main frame and the left- and right-hand insets present curve sets, which correspond to curves C, B, and A of Fig. 9, respectively.

Conductance-voltage curves $G(V)$s for several junctions showing surface superconductivity are displayed in Fig. 9 to confirm the reproducibility using BJ. Curve A possesses kink structures at ±7 mV with a zero-bias broad hump. Additional maxima are seen inside the hump at ±3.5 mV, below which the hump becomes narrower. Such a behavior can be related to the superconductivity, which may be a consequence of the SNS junction formation and the appearance of the Saint-James-Andreev reflection (SJAR) [111]. The inner kinks at ±3.5 mV, which are half of the outer kinks ±7 mV, are naturally attributed to the subharmonic gap structure at $\pm\Delta/e$. Very weak slope changes are scarcely seen at ±2 mV. These values may be attributed to the subharmonic gap structures at the biases $V = \pm(2\Delta/e)/n$ caused by the multiple SJAR. Here n denotes the integer numbers. It is known that the numbers of structure depend on l/d, where l and d are the mean free path of the electron and the normal region thickness between the superconductor electrodes, respectively [111–113]. In the low bias region, the numbers n of SJAR is limited by l according to the relationship $n = l/d$. From the clearly visible numbers of kinks $n = 2$ in Fig. 9, curve A, normal-region thickness can be estimated as $d \approx 5$ nm assuming $l \approx 10$ nm for the cuprate superconductor. Similar conductance features of SJAR can be seen elsewhere [113].

In curves B, C, and D, broad maxima appear at ±7 mV, i.e., at locations of the minima with $n = 1$ in curve A. In curve B, the trend to form a gap-like depression below ±6–7 mV is interrupted by the appearance of a huge Josephson-like conductance peak with an additional shallow and narrow dip at $V = 0$. This feature is followed by the extra structure at $\pm \sim 10$–12 mV. This extra structure is similar to those observed in the weak-link junctions. The featureless gap inside broad peaks in curves C and D differs substantially from the rich inner structure of curve B, indicating a dominant quasiparticle tunneling. In fact, curve C is described by the quasiparticle density of states Eq. (1) as indicated in Fig. 9. Curve E is the low-V blow-up of curve H from Fig. 3. It clearly demonstrates the coexistence of CDWs and superconductivity in the freshly fractured surface of $Sr_{2.5}Ca_{11.5}Cu_{24}O_{41}$. The superconducting gap can be seen only in the positive bias branch. However, its location at +7 mV agrees well with the data for BJs A, B, C, and D. As for the absence of the accompanying gap feature at −7 mV, it might be due to the obscuring influence of the power-law background, which also occurs in tunnel junctions made of various materials and the nature of which is not known for sure [64,70,89]. Therefore, the data represented by curve E are consistent with those describing other BJs and depicted in Fig. 9.

Thermal evolution of $G(V)$s from Fig. 9 is demonstrated in Fig. 10. The features related to superconductivity of curves A and B from Fig. 9 disappear at ∼7–7.3 K, as is shown in the inset of Fig. 10. This closing temperature is approximately the same as that shown in Fig. 8, although the low-T gap values from the inset are almost two times larger than those of Fig. 8. The low-T spikes in curve B vanishing at the same T_c indicate the same origin of the features concerned. In the main frame of Fig. 10, the T-evolution of curve C in Fig. 9 is depicted. The broad gap-edge peaks gradually disappear near ∼7.5 K. The fact that the distinct structure quickly disappears at such low T is similar to the data of A and B, which can be related to

the surface superconductivity. The disappearance of a distinct gap structure at T being much lower than its mean-field value seems unusual, but it was often observed in BJ of other superconductors such as Fe(Se,Te) [114]. In curve C, however, the zero-bias depression persists above this temperature and merges into the background at ≈12.4 K. It is remarkable that this value is very close to the $T_c = 12$ K found in this material under the pressure of 3.5 GPa [1,2]. If we consider 12.4 K as the true critical temperature of the surface superconducting transition and identify the peak-to-peak distance in curve C as $4\Delta(4\text{ K}) \approx 16$ meV, the ratio $2\Delta(0)/k_BT_c$ can be estimated as ∼7.5.

This is consistent with the ratio $2\Delta(0)/k_BT_c$ for the weaker superconductivity with lower $T_c \approx 7$ K and 4Δ (4 K) ≈8 meV for BJs displayed in Fig. 8. It suggests a similar nature of superconducting manifestations in different samples.

To observe the surface atomic structure responsible for superconductivity, we used the STM at $T = 4.9$ K to image the crystal surface topography for the $Sr_{2.5}Ca_{11.5}Cu_{24}O_{41}$ crystal and applied the fast-Fourier-transform (FFT) method to construct the corresponding map. They are shown in Figs. 11(a) and 11(b), respectively. The crystal was cleaved *in situ* at 77 K in UHV. The step-like character of the cleaved surface renders the observation of regular atomic lattice arrangements impossible. Similar distorted surface atomic arrangements were also observed, e.g., in the layered superconductor MgB_2, thus seeming to be a common feature inherent to mechanically cleaved surfaces [31,32]. The arrangements of sub-nm spots are clearly seen in the region of 6.4 nm × 6.4 nm in Fig. 11(a), in which the bright spots are randomly distributed over the surface. We observed a similar STM image in almost every surface region, in which a tiny crystal piece was torn off and the surface was exposed at low T. Thereby, we believe that typical and fresh surface domains are observed. As for the effective tunneling region, typical break-junction sampling area was estimated as $\approx 10^{-10}$–10^{-11} mm^2 for the superconducting tunneling [107], which suggests that the effective size of the present STM area differs insignificantly from the break-junction sampling interface.

It is reasonable to associate the size of the observed spot with the type of the atom. Among the well-defined spots, the vertical heights of the bright atomic spots are distributed in the range of 0.07–0.10 nm from the background surface, which is roughly consistent with the radius 0.07–0.08 nm of a Cu ion. The FFT analysis of Fig. 11(b) reveals a central halo and spots below the reciprocal length ∼1 nm^{-1}, but those spots should be attributed to the irregular surface modulation created by cleavage, as is seen from Fig. 11(a). Those features are not associated with the intrinsic surface characteristics in the reciprocal space.

After the removal of irrelevant features, the bright-spot Cu spacing of 0.39_6 nm, and other characteristic lengthscales of nm, 0.70_3 nm, and 0.71_1 nm are recognized. The value of 0.58_1 nm corresponds to the diagonal length between Sr sites. Since vectors of 0.70_3 nm and 0.71_1 nm lengths align along the same directions as those of 0.39_6 nm and 0.58_1 nm ones, respectively, the first ones correspond to the superlattice modulations, with spatial periods being ≈1.78 and ≈1.22 times the Cu-Cu and Sr-Sr atomic spacings, respectively. The detected superstructures (CDWs) can be most

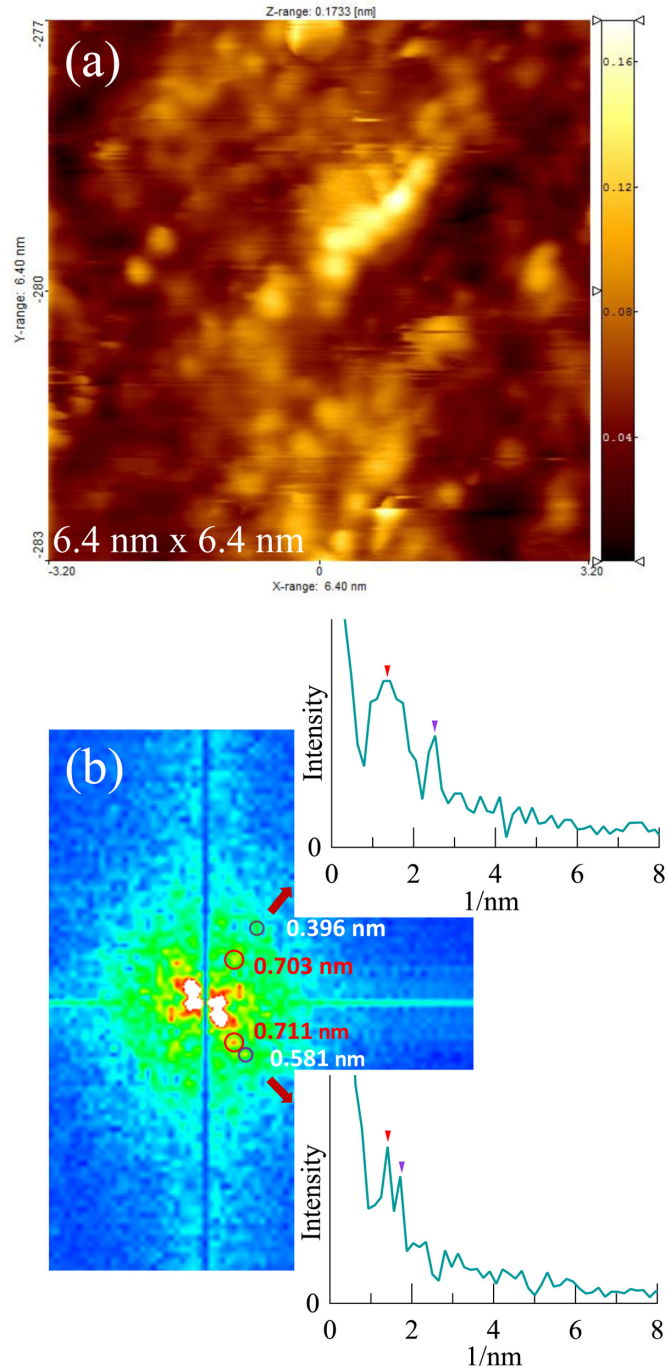

FIG. 11. (a) The topography of the cleaved surface of $Sr_{2.5}Ca_{11.5}Cu_{24}O_{41}$ (sample bias $V = +0.4$ V, current $I = 0.4$ nA, $T = 4.9$ K) revealed by low-temperature ultra-high-vacuum scanning tunneling microscopy (LT-UHV-STM). (b) The corresponding fast-Fourier-transform (FFT) map.

probably the origin of the dielectric gapping in the ladder compound. The same kind of features are responsible for the normal-state gap formation in cuprate high T_c superconductors [21,22,62,64,83,115].

It should be emphasized once more that there are neither single elements nor binary or ternary compounds composed of the elements constituting the ladder compound $(Sr,Ca)_{14}Cu_{24}O_{41}$, which exhibit superconductivity at ambient

pressure with T_c higher than the liquid helium boiling temperature 4.2 K. Moreover, the compound concerned becomes superconducting only at high pressures larger than 3–5 GPa [1,2,6,15]. Therefore, phenomena presented here in Figs. 6 to 10 are clear-cut manifestations of the ambient pressure surface superconductivity emerging in the interface regions of BJs.

As was indicated in the Introduction, the search for superconductivity driven by the apparent difference between electron properties in the bulk and near the surface of a crystal lasts for a long time [53,54]. The first idea was to implement a nonphonon mechanism of Cooper pairing, for instance, an exciton one, when the surface added certain degrees of freedom [116–122]. This possibility cannot be excluded even now, although there are still no proofs that such fully electronic superconductivity mechanisms do exist in nature.

Another very compelling reason for enhanced or emerging superconductivity at the interface is a possibility of a larger concentration of charge carriers (and the electron density of states as a consequence) near the boundary between adjacent media. It might be intentional charge injection, as was proposed several decades ago [123,124] and practically realized [125]. Superconductivity may be also induced by the inevitable inner contact potential at the interface between two conducting solids [126]. In our case it might be realized inside the BJ area, where random inhomogeneity leads to the unpredictable distribution of electron densities of states and effective Cooper-pairing interaction constants [64].

Superconductivity originating from the electron-phonon interaction (which is the only one proved to exist, for now) may be specifically stimulated near the surface due to the additional or enhanced peculiarities of the electron spectrum in the two-dimensional case [127–130]. For instance, one can mention giant Kohn anomalies [131], Peierls transition [21,97,99,132], electron spectrum Van Hove singularities [133].

Our observations of the interface mean-field-like superconductivity [55,56,60,80] (rather than the BKT one [57]) agree well with the familiar fact of the superconductivity persistence in single layers of $NbSe_2$ [134] and the general robustness of dichalcogenide superconductivity against intercalation with organic molecules [135–140]. At the moment, many other atomic-thick two-dimensional superconductors were discovered, including ultra-thin metallic films, surface superstructures, and moiré-graphene superlattices [141–143].

In our context, it is especially important that two-dimensional superconductivity was realized in epitaxial structures consisting of high-T_c cuprate layers [144–148]. Such interface superconductivity was found in other systems as well [141,148]. It is of no wonder because the nature of superconductivity in already known materials reveals common features based on the Cooper pairing concept. We do not know for sure the boson glue binding electrons into loose pairs. Nevertheless, the absence of the transition-element atoms in the hydrogen-sulfur compound exhibiting high-temperature under pressure [149] suggests that the electron-phonon mechanism is at least dominant [32].

The noncuprate interface-superconductivity systems include FeSe monolayer on $SrTiO_3$ substrate [150–152]. Here, truly high T_c is above 100 K, whereas the bulk FeSe exhibits superconductivity only at about 8 K at ambient pressure enhanced to 37 K under the pressure [153] and the doped oxide $SrTiO_3$ has an extremely low charge carrier concentration and small $T_c \lesssim 0.45$ K [154]. Those data testify that the mechanical influence may increase T_c drastically. In this connection, it is worthwhile to mention the layered transition-metal dichalcogenide $MoTe_2$, recognized as a Weyl semimetal, which possesses $T_c \approx 0.1$ K at ambient pressure, gaining much higher $T_c \approx 8.2$ K by applying the pressure of 11.7 GPa [155]. More interestingly, recent point contact measurements of $MoTe_2$ revealed the surface superconductivity having the critical temperature ≈5 K, which is substantially higher than the bulk one [156]. Another binary oxide structure exhibiting the interface superconductivity is $LaAlO_3/SrTiO_3$ [141,154]. However, here $T_c \approx 0.2$ K is tiny and is considered as a manifestation of the BKT state. At the same time, in $CaCuO_2/SrTiO_3$ heterostructures that include two constituents, being insulating taken separately, $T_c \approx 38$ K of the interface superconductivity is indeed very high [157]. It seems that here the cuprate component plays a positive role.

Returning to our experiments, we note that, to our knowledge, $T_c < 6$ K was never reported for cuprate superconductors [158–160]. Therefore, we suggest a hypothesis that it might be regarded as the lowest value characterizing this class of materials. Our $T_c \approx 7$ K for $Sr_{2.5}Ca_{11.5}Cu_{24}O_{41}$ is close to this value. Moreover, our previous BJTS measurements revealed $T_c \approx 6$–7 K in the inhomogeneous compositions of $La_{2-x}Sr_xCuO_4$ with $x = 0.15$ and 0.05 showing a possible lower T_c [161]. Of course, surface (interface) superconductivity is a more general phenomenon than that concerning cuprates and even other oxides [162]. The cited data for dichalcogenides support this viewpoint. Furthermore, it turned out that the enhanced surface superconductivity is built-in into its bulk counterpart, the both coexisting in the same sample [163]. Finally, the substrate-induced doping has been recently shown to create superconductivity in the Sn layer adsorbed on the *p*-type Si (111) wafer [164]. The Van Hove singularity clearly shown up in the tunneling spectra measured in this system is highly suspicious to be responsible for the superconducting pairing.

To summarize, the surface or interface superconductivity found here may originate either from the two-dimensional specificity of the BJ interfaces or from the junction-material inhomogeneity. The inhomogeneity may realize the random network favorable for emerging superconductivity. For instance, it can occur in the framework of the electronic self-organized percolation scenario [165,166]. The unexpected surface superconductivity and expected CDWs were demonstrated to coexist in the studied composition $Sr_{2.5}Ca_{11.5}Cu_{24}O_{41}$ of the ladder-chain oxide. They manifest themselves on substantially different scales. Therefore, we were able to study those competing phenomena separately and no interplay between them was found.

IV. SUMMARY

BJ tunneling measurements at ambient pressure of the ladder-chain compound $Sr_{2.5}Ca_{11.5}Cu_{24}O_{41}$ demonstrated $G(V)$ involving both semiconducting (CDW) and interface superconducting gaps. The semiconducting gap $2\Sigma(4\text{ K})$ values are mainly in the range of ≈100–150 meV. The gap

disappears at temperatures $T^* \approx 90$–100 K, resulting in the ratio $2\Sigma(0)/k_BT^* \sim 14$–$19$. Similar large ratios are known for other materials exhibiting CDW transition, e.g., $NbSe_3$. The overall T dependence $\Sigma(T)$ differs substantially from the mean-field behavior, most probably due to the order parameter fluctuations. At low T, a sharp zero-bias peak is observed and attributed to the Josephson effect. The superconducting gap is observed at fresh BJ interfaces, the amplitude of which is most often $2\Delta(4\text{ K}) \approx 4$ meV, but for certain junctions extending up to 8 meV. These surface superconducting gaps disappear at critical temperatures $T_c \approx 7$–8 K, although the low-bias depression merges with the background at about 12.4 K. The characteristic ratio $2\Delta(0)/k_BT_c$ is in the range $\approx 7 \pm 0.5$. The STM measurements were carried out and resolved surface atomic arrangements on the cracked surface, being blurred by substantial distortions. These distortions might be related to the emergence of the surface superconductivity.

ACKNOWLEDGMENTS

We would like to thank the Natural Science Center for Basic Research and Development, Hiroshima University for supplying liquid helium and the EPMA element analysis. This research was supported by Grant-in-Aid for Scientific Research Grants No. 19540370 and No. 245403770 from JSPS, Japan and Grants No. 1.4.B-197, No. VC-188, and No. VC-16 of the Institute of Physics of the National Academy of Sciences of Ukraine.

[1] M. Uehara, T. Nagata, J. Akimitsu, H. Takahashi, N. Mohri, and K. Kinoshita, J. Phys. Soc. Jpn. **65**, 2764 (1996).
[2] T. Vuletić, B. Korin-Hamzić, T. Ivek, S. Tomić, B. Gorshunov, M. Dressel, and J. Akimitsu, Phys. Rep. **428**, 169 (2006).
[3] C. W. Chu, L. Z. Deng, and B. Lv, Physica C **514**, 290 (2015).
[4] E. M. McCarron III, M. A. Subramanian, J. C. Calabrese, and R. L. Harlow, Mat. Res. Bull. **23**, 1355 (1988).
[5] N. Motoyama, T. Osafune, T. Kakeshita, H. Eisaki, and S. Uchida, Phys. Rev. B **55**, R3386 (1997).
[6] T. Nagata, M. Uehara, J. Goto, J. Akimitsu, N. Motoyama, H. Eisaki, S. Uchida, H. Takahashi, T. Nakanishi, and N. Môri, Phys. Rev. Lett. **81**, 1090 (1998).
[7] H. Stern, Phys. Rev. B **8**, 5109 (1973).
[8] H. Stern, Phys. Rev. B **12**, 951 (1975).
[9] C. Buzea and K. Robbie, Supercond. Sci. Technol. **18**, R1 (2005).
[10] A. J. Leggett, Annu. Rev. Condens. Matter Phys. **2**, 11 (2011).
[11] G. W. Webb, F. Marsiglio, and J. E. Hirsch, Physica C **514**, 17 (2015).
[12] K. Conder, Supercond. Sci. Technol. **29**, 080502 (2016).
[13] E. Dagotto, J. Riera, and D. Scalapino, Phys. Rev. B **45**, 5744 (1992).
[14] P. W. Anderson, Phys. Rev. Lett. **34**, 953 (1975).
[15] N. Motoyama, H. Eisaki, S. Uchida, N. Takeshita, N. Môri, T. Nakanishi, and H. Takahashi, Europhys. Lett. **58**, 758 (2002).
[16] T. Osafune, N. Motoyama, H. Eisaki, and S. Uchida, Phys. Rev. Lett. **78**, 1980 (1997).
[17] P. Abbamonte, G. Blumberg, A. Rusydi, A. Gozar, P. G. Evans, T. Siegrist, L. Venema, H. Eisaki, E. D. Lsaacs, and G. G. Sawatzky, Nature (London) **431**, 1078 (2004).
[18] T. Vuletić, T. Ivek, B. Korin-Hamzić, S. Tomic, B. Gorshunov, P. Haas, M. Dressel, J. Akimitsu, T. Sasaki, and T. Nagata, Phys. Rev. B **71**, 012508 (2005).
[19] A. Rusydi, W. Ku, B. Schulz, R. Rauer, I. Mahns, D. Qi, X. Gao, A. T. S. Wee, P Abbamonte, H. Eisaki, Y. Fujimaki, S. Uchida, and M. Rubhausen, Phys. Rev. Lett. **105**, 026402 (2010).
[20] R. H. Friend and D. Jerome, J. Phys. C: Solid State **12**, 1441 (1979).
[21] A. M. Gabovich, A. I. Voitenko, and M. Ausloos, Phys. Rep. **367**, 583 (2002).
[22] A. M. Gabovich, A. I. Voitenko, T. Ekino, M. S. Li, H. Szymczak, and M. Pękała, Adv. Condens. Matter Phys. **2010**, 681070 (2010).
[23] F. Denoyer, R. Comes, A. F. Garito, and A. J. Heeger, Phys. Rev. Lett. **35**, 445 (1975).
[24] E. Wigner, Trans. Faraday Soc. **34**, 678 (1938).
[25] D. J. Scalapino, Phys. Rep. **250**, 329 (1995).
[26] A. Abanov, A. V. Chubukov, and J. Schmalian, J. Electron Spectrosc. Relat. Phenom. **117**, 129 (2001).
[27] H. Mukuda, S. Shimizu, A. Iyo, and Y. Kitaoka, J. Phys. Soc. Jpn. **81**, 011008 (2012).
[28] E. Dagotto and T. M. Rice, Science **271**, 618 (1996).
[29] J. Moreland and J. W. Ekin, J. Appl. Phys. **58**, 3888 (1985).
[30] T. Ekino, T. Takabatake, H. Tanaka, and H. Fujii, Phys. Rev. Lett. **75**, 4262 (1995).
[31] A. Sugimoto, Y. Yanase, T. Ekino, Y, Muranaka, and A. M. Gabovich, Low Temp. Phys. **45**, 1209 (2019).
[32] A. Sugimoto, M. Iwano, S. Ishimitsu, T. Ekino, and A. M. Gabovich, Supercond. Sci. Technol. **33**, 095011 (2020).
[33] J. J. Hamlin, Physica C **514**, 59 (2015).
[34] B. Raveau, Phys. Today **45**(10), 53 (1992).
[35] R. J. Cava, J. Am. Ceram. Soc. **83**, 5 (2000).
[36] A. Kiejna and K. F. Wojciechowski, *Metal Surface Electron Physics* (Pergamon, Oxford, 1996).
[37] W. Monch, *Semiconductor Surfaces and Interfaces*, 3rd ed. revised (Springer, Berlin, 2001).
[38] H. Ibach, *Physics of Surfaces and Interfaces* (Springer, Berlin, 2006).
[39] K. Oura, V. G. Lifshits, A. A. Saranin, A. V. Zotov, and M. Katayama, *Surface Science: An Introduction* (Springer, Berlin, 2003).
[40] J. E. Inglesfield, Progr. Surf. Sci. **20**, 105 (1985).
[41] B. Meyer and D. Vanderbilt, Phys. Rev. B **63**, 205426 (2001).
[42] R. T. Tung, Mater. Sci. Eng. R **35**, 1 (2001).
[43] J. Goniakowski, F. Finocchi, and C. Noguera, Rep. Prog. Phys. **71**, 016501 (2008).
[44] M. Faraday, Proc. R. Soc. London **10**, 440 (1859).
[45] J. S. Wettlaufer, Phil. Trans. R. Soc. Lond. A **357**, 1763 (1999).
[46] B. Slater and A. Michaelides, Nat. Rev. Chem. **3**, 172 (2019).
[47] I. Tamm, Z. Phys. **76**, 849 (1932).
[48] W. Shockley, Phys. Rev. **56**, 317 (1939).

[49] J. D. Patterson and B. C. Bailey, *Solid-State Physics: Introduction to the Theory*, 3rd ed. (Springer, Berlin, 2010).

[50] M. Stęślicka, Prog. Surf. Sci. **5**, 157 (1974).

[51] *The Chemical Physics of Solid Surfaces*, Vol. 9, Oxide Surfaces, edited by D. P. Woodruff (Elsevier, Amsterdam, 2001).

[52] R. M. Osgood, Jr. and X. Wang, in *Solid State Physics: Advances in Research and Applications*, edited by H. Ehrenreich and F. Spaepen (Academic, San Diego, 1998), pp. 1–80.

[53] V. L. Ginzburg and D. A. Kirzhnits, Sov. Phys. JETP **19**, 269 (1964).

[54] V. L. Ginzburg, Phys. Lett. **13**, 101 (1964).

[55] J. Bardeen, L. N. Cooper, and J. R. Schrieffer, Phys. Rev. **108**, 1175 (1957).

[56] J. F. Annett, *Superconductivity, Superfluids and Condensates* (Oxford University Press, Oxford, 2004).

[57] J. M. Kosterlitz, Rep. Prog. Phys. **79**, 026001 (2016).

[58] U. Ammerahl, G. Dhalenne, A. Revcolevschi, J. Berthon, and H. Mouddon, J. Cryst. Growth **193**, 55 (1998).

[59] I. Giaever and K. Megerle, Phys. Rev. **122**, 1101 (1961).

[60] A. Barone and G. Paterno, *The Physics and Applications of the Josephson Effect* (John Wiley and Sons, New York, 1982).

[61] C. Wang, B. Giambattista, C. G. Slough, R. V. Coleman, and M. A. Subramanian, Phys. Rev. B **42**, 8890 (1990).

[62] T. Ekino, Y. Sezaki, and H. Fujii, Phys. Rev. B **60**, 6916 (1999).

[63] T. Ekino, A. Sugimoto, A. M. Gabovich, R. Sekine, K. Tanabe, and K. Tokiwa, J. Energy Challenges and Mechanics **5**, 1 (2018).

[64] T. Ekino, A. M. Gabovich, M. S. Li, H. Szymczak, and A. I. Voitenko, Low Temp. Phys. **46**, 400 (2020).

[65] J. C. Phillips, Phys. Rev. B **71**, 184505 (2005).

[66] J.-X. Li, C.-Q. Wu, and D.-H. Lee, Phys. Rev. B **74**, 184515 (2006).

[67] W. D. Wise, M. C. Boyer, K. Chatterjee, T. Kondo, T. Takeuchi, H. Ikuta, Y. Wang, and E. W. Hudson, Nat. Phys. **4**, 696 (2008).

[68] B. Loret, N. Auvray, G. D. Gu, A. Forget, D. Colson, M. Cazayous, Y. Gallais, I. Paul, M. Civelli, and A. Sacuto, Phys. Rev. B **101**, 214520 (2020).

[69] T. Ekino, A. M. Gabovich, Mai Suan Li, H. Szymczak, and A. I. Voitenko, J. Phys.: Condens. Matter **29**, 505602 (2017).

[70] T. Takasaki, T. Ekino, H. Fujii, and S. Yamanaka, J. Phys. Soc. Japan **74**, 2586 (2005).

[71] K. P. Rajeev, G. V. Shivashankar, and A. K. Raychaudhuri, Solid State Commun. **79**, 591 (1991).

[72] B. L. Altshuler and A. G. Aronov, in *Electron-Electron Interactions in Disordered Systems*, edited by A. L. Efros and M. Pollak (North-Holland, Amsterdam, 1985), pp. 1–153.

[73] P. A. Lee and T. V. Ramakrishnan, Rev. Mod. Phys. **57**, 287 (1985).

[74] A. K. Raychaudhuri, Adv. Phys. **44**, 21 (1995).

[75] T. Ekino and J. Akimitsu, Physica B **194**, 1221 (1994).

[76] X.-Z. Huang and K. Maki, Phys. Rev. B **40**, 2575 (1989).

[77] U. Staufer, R. Wiesendanger, L. Eng, L. Rosenthaler, H. R. Hidber, H. J. Güntherodt, and N. Garcia, J. Vac. Sci. Technol. A **6**, 537 (1988).

[78] R. Wiesendanger, Appl. Surf. Sci. **54**, 271 (1992).

[79] R. C. Dynes, V. Narayanamurti, and J. P. Garno, Phys. Rev. Lett. **41**, 1509 (1978).

[80] E. L. Wolf, *Principles of Tunneling Spectroscopy* (Oxford University Press, Oxford, 2012).

[81] M. R. Presland, J. L. Tallon, R. G. Buckley, R. S. Liu, and N. E. Flower, Physica C **176**, 95 (1991).

[82] T. Ekino and J. Akimitsu, Jpn. J. Appl. Phys. **26**, 625 (1987).

[83] T. Ekino, S. Hashimoto, T. Takasaki, and H. Fujii, Phys. Rev. B **64**, 092510 (2001).

[84] Yu. I. Latyshev, P. Monceau, S. Brazovskii, A. P. Orlov, and T. Fournier, Phys. Rev. Lett. **95**, 266402 (2005).

[85] J. R. Cooper and A. G. F. Wyatt, J. Phys. F **3**, L120 (1973).

[86] W. F. Brinkman, R. C. Dynes, and J. M. Rowell, J. Appl. Phys. **41**, 1915 (1970).

[87] J. W. Conley, C. B. Duke, G. D. Mahan, and J. J. Tiemann, Phys. Rev. **150**, 466 (1966).

[88] C. H. Ahn, A. Bhattacharya, M. Di Ventra, J. N. Eckstein, C. D. Frisbie, M. E. Gershenson, A. M. Goldman, I. H. Inoue, J. Mannhart, A. J. Millis, A. F. Morpurgo, D. Natelson, and J.-M. Triscone, Rev. Mod. Phys. **78**, 1185 (2006).

[89] J. R. Kirtley and D. J. Scalapino, Phys. Rev. Lett. **65**, 798 (1990).

[90] G. Grüner, *Density Waves in Solids* (Addison-Wesley, Reading, MA, 1994).

[91] J. Kawabata, T. Ekino, Y. Yamada, Y. Sakai, A. Sugimoto, Y. Muro, and T. Takabatake, Phys. Rev. B **92**, 201113(R) (2015).

[92] B. Renker, L. Pintschovius, W. Glaser, H. Rietschel, R. Comes, L. Liebert, and W. Drexel, Phys. Rev. Lett. **32**, 836 (1974).

[93] J. W. Lynn, M. Iizumi, G. Shirane, S. A. Werner, and R. B. Saillant, Phys. Rev. B **12**, 1154 (1975).

[94] M. Thielemans, R. Deltour, D. Jerome, and J. R. Cooper, Solid State Commun. **19**, 21 (1976).

[95] D. J. Scalapino, M. Sears, and R. A. Ferrel, Phys. Rev. B **6**, 3409 (1972).

[96] P. A. Lee, T. M. Rice, and P. W. Anderson, Phys. Rev. Lett. **31**, 462 (1973).

[97] M. J. Rice and S. Strässler, Solid State Commun. **13**, 1389 (1973).

[98] W. Dieterich, Adv. Phys. **25**, 615 (1976).

[99] P. Monceau, Adv. Phys. **61**, 325 (2012).

[100] T. Vuletić, B. Korin-Hamzić, S. Tomić, B. Gorshunov, P. Haas, T. Rõõm, M. Dressel, J. Akimitsu, T. Sasaki, and T. Nagata, Phys. Rev. Lett. **90**, 257002 (2003).

[101] B. D. Josephson, Phys. Lett. **1**, 251 (1962).

[102] C. M. Falco, W. H. Parker, and S. E. Trullinger, Phys. Rev. B **10**, 1865 (1974).

[103] V. Ambegaokar and A. Baratoff, Phys. Rev. Lett. **10**, 486 (1963).

[104] A. Sugimoto, H. Ohtsubo, K. Matsumoto, S. Ishimitsu, M. Iwano, T. Ekino, and A. M. Gabovich, J. Phys. Conf. Ser. **1975**, 012005 (2021).

[105] A. M. Gabovich, D. P. Moiseev, A. S. Shpigel, and A. I. Voitenko, Phys. Stat. Sol. (b) **161**, 293 (1990).

[106] A. M. Gabovich and A. I. Voitenko, Low Temp. Phys. **39**, 232 (2013).

[107] T. Ekino, H. Fujii, M. Kosugi, Y. Zenitani, and J. Akimitsu, Phys. Rev. B **53**, 5640 (1996).

[108] T. Ekino, T. Takasaki, T. Muranaka, J. Akimitsu, and H. Fujii, Phys. Rev. B **67**, 094504 (2003).

[109] Yu. S. Barash, A. V. Galaktionov, and A. D. Zaikin, Phys. Rev. Lett. **75**, 1676 (1995).
[110] M. Ledvij and R. A. Klemm, Phys. Rev. B **51**, 3269 (1995).
[111] G. E. Blonder, M. Tinkham, and T. M. Klapwijk, Phys. Rev. B **25**, 4515 (1982).
[112] R. Kümmel, U. Gunsenheimer, and R. Nicolsky, Phys. Rev. B **42**, 3992 (1990).
[113] P. I. Bezotosnyi, K. A. Dmitrieva, A. V. Sadakov, K. S. Pervakov, A. V. Muratov, A. S. Usoltsev, A. Yu. Tsvetkov, S. Yu. Gavrilkin, N. S. Pavlov, A. A. Slobodchikov, O. Yu. Vilkov, A. G. Rybkin, I. A. Nekrasov, and V. M. Pudalov, Phys. Rev. B **100**, 184514 (2019).
[114] T. Ekino, A. Sugimoto, and A. M. Gabovich, IOP Conf. Ser.: Mater. Sci. Eng. **369**, 012024 (2018).
[115] A. M. Gabovich and A. I. Voitenko, Phys Rev. B **80**, 224501 (2009).
[116] W. A. Little, Phys. Rev. **134**, A1416 (1964).
[117] V. L. Ginzburg, Annu. Rev. Mater. Sci. **2**, 663 (1972).
[118] D. Allender, J. Bray, and J. Bardeen, Phys. Rev. B **7**, 1020 (1973).
[119] A. M. Gabovich, E. A. Pashitskii, and S. K. Uvarova, Sov. J. Low Temp. Phys. **1**, 473 (1975).
[120] D. Davis, H. Gutfreund, and W. A. Little, Phys. Rev. B **13**, 4766 (1976).
[121] E. G. Maksimov and O. V. Dolgov, Physics Usp. **50**, 933 (2007).
[122] G. R. Stewart, Adv. Phys. **66**, 75 (2017).
[123] B. Y. Shapiro, Sov. Phys. JETP **61**, 998 (1985).
[124] B. Ya. Shapiro, Phys. Rev. B **48**, 16722 (1993).
[125] G. Dubuis, A. T. Bollinger, D. Pavuna, and I. Božović, J. Appl. Phys. **111**, 112632 (2012).
[126] B. Y. Shapiro, Phys. Stat. Sol. (b) **129**, 359 (1985).
[127] J. E. Hirsch and D. J. Scalapino, Phys. Rev. Lett. **56**, 2732 (1986).
[128] J. Kröger, Rep. Prog. Phys. **69**, 899 (2006).
[129] A. Moor, A. F. Volkov, and K. B. Efetov, Phys. Rev. B **91**, 064511 (2015).
[130] S. H. Liu and R. A. Klemm, Phys. Rev. B **52**, 9657 (1995).
[131] H. Rietschel, Solid State Commun. **13**, 1859 (1973).
[132] A. J. Berlinsky, Rep. Prog. Phys. **42**, 1243 (1979).
[133] R. S. Markiewicz, J. Phys. Chem Sol. **58**, 1179 (1997).
[134] R. F. Frindt, Phys. Rev. Lett. **28**, 299 (1972).
[135] R. A. Klemm, *Layered Superconductors*, Vol. 1 (Oxford University Press, Oxford, 2012).
[136] R. A. Klemm, Physica C **514**, 86 (2015).
[137] F. R. Gamble, F. J. DiSalvo, R. A. Klemm, and T. H. Geballe, Science **168**, 568 (1970).
[138] F. R. Gamble, J. H. Osiecki, M. Cais, R. Pisharody, F. J. DiSalvo, and T. H. Geballe, Science **174**, 493 (1971).
[139] F. R. Gamble and A. H. Thompson, Solid State Commun. **27**, 379 (1978).
[140] R. H. Friend and A. D. Yoffe, Adv. Phys. **36**, 1 (1987).
[141] T. Uchihashi, Supercond. Sci. Technol. **30**, 013002 (2017).
[142] T. Nakamura, H. Kim, S. Ichinokura, A. Takayama, A. V. Zotov, A. A. Saranin, Y. Hasegawa, and S. Hasegawa, Phys. Rev. B **98**, 134505 (2018).
[143] L. Balents, C. R. Dean, D. K. Efetov, and A. F. Young, Nat. Phys. **16**, 725 (2020).
[144] I. Božović, J. N. Eckstein, M. E. Klausmeier-Brown, and G. Virshup, J. Supercond. **5**, 19 (1992).
[145] A. T. Bollinger and I. Božović, Supercond. Sci. Technol. **29**, 103001 (2016).
[146] V. A. Gasparov, L. Drigo, A. Audouard, X. He, and I. Božović, Phys. Rev. B **94**, 014507 (2016).
[147] G. Logvenov, A. Gozar, and I. Božović, Science **326**, 699 (2009).
[148] L. Wang, X. Ma, and Q.-K. Xue, Supercond. Sci. Technol. **29**, 123001 (2016).
[149] C. J. Pickard, I. Errea, and M. I. Eremets, Annu. Rev. Condens. Matter Phys. **11**, 57 (2020).
[150] J. F. Ge, Z. L. Liu, C. Liu, C. L. Gao, D. Qian, Q. K. Xue, Y. Liu, and J. F. Jia, Nat. Mater. **14**, 285 (2015).
[151] D. Huang and J. E. Hoffman, Annu. Rev. Condens. Matter Phys. **8**, 311 (2017).
[152] A. Gozar and I. Božović, Physica C **521**, 38 (2016).
[153] X. Liu, L. Zhao, S. He, J. He, D. Liu, D. Mou, B. Shen, Y. Hu, J. Huang, and X. J. Zhou, J. Phys.: Condens. Matter **27**, 183201 (2015).
[154] Y.-Y. Pai, A. Tylan-Tyler, P. Irvin, and J. Levy, Rep. Prog. Phys. **81**, 036503 (2018).
[155] V. Süss, M. Schmidt, U. Schwarz, E. Pippel, P. Werner, R. Hillebrand, T. Förster, E. Kampert, S. Parkin, R.J. Cava, C. Felser, B. Yan, and A. Medvedev Nat. Commun. **7**, 11038 (2016).
[156] Y. Naidyuk, O. Kvitnitskaya, D. Bashlakov, S. Aswartham, I. Morozov, I. Chernyavskii, G. Fuchs, S. L. Drechsler, R. Hühne, K. Nielsch, B. Büchner, and D. Efremov, 2D Mater. **5**, 045014 (2018).
[157] D. Di Castro, C. Cantoni, F. Ridolfi, C. Aruta, A. Tebano, N. Yang, and G. Balestrino, Phys. Rev. Lett. **115**, 147001 (2015).
[158] T. Ekino and J. Akimitsu, Phys. Rev. B **40**, 6902 (1989).
[159] T. Ekino, Y. Sezaki, H. Umeda, and H. Fujii, *Advances in Superconductivity X* (Springer, New York, 1998), p. 183.
[160] T. Ekino, Y. Sezaki, and H. Fujii, *Advances in Superconductivity XI* (Springer, New York, 1999), p. 169.
[161] T. Ekino, T. Doukan, H. Fujii, F. Nakamura, S. Sakita, M. Kodama, and T. Fujita, Physica C **263**, 249 (1996).
[162] C. W. Chu, L. Z. Deng, M. Gooch, S. Y. Huyan, B Lv, and Z. Wu, J. Supercond. Novel Magn. **32**, 7 (2019).
[163] F. Levy-Bertrand, B. Michon, J. Marcus, C. Marcenat, J. Kačmarčík, T. Klein, and H. Cercellier, Physica C **523**, 19 (2016).
[164] X. Wu, F Ming, T. S. Smith, G. Liu, F. Ye, K. Wang, S. Johnston, and H. H. Weitering, Phys. Rev. Lett. **125**, 117001 (2020).
[165] J. C. Phillips, A. Saxena, and A. R. Bishop, Rep. Prog. Phys. **66**, 2111 (2003).
[166] J. C. Phillips, Chem. Phys. Lett. **473**, 274 (2009).